GaAs spectrometer for planetary electron spectroscopy

Article (Accepted Version)

GaAs Spectrometer for Planetary Electron Spectroscopy

G. Lioliou, S. Butera, S. Zhao, M.D.C. Whitaker, and A.M. Barnett

Space Research Group, Sch. of Engineering and Informatics, University of Sussex, Falmer, Brighton, BN1 9QT, UK

Corresponding author: G. Lioliou (G.Lioliou@sussex.ac.uk)

Key Points:

- A radiation-hard direct detection electron spectrometer employing a GaAs detector is reported. It functions at temperatures up to 100 °C.
- Space missions to extreme environments may benefit from such an instrument.
- The use of the spectrometer for measuring the soft (≤ 100 keV) electron environment at Europa is modelled.

Abstract

Work towards producing a radiation-hard and high temperature tolerant direct detection electron spectrometer is reported. The motivation is to develop a low-mass, low-volume, low-power, multi-mission capable instrument for future space science missions. The resultant prototype electron spectrometer employed a GaAs p^+-i-n^+ mesa photodiode (10 μm i layer thickness; 200 μm diameter) and a custom-made charge-sensitive preamplifier. The GaAs detector was initially electrically characterized as a function of temperature. The detector-preamplifier assembly was then investigated for its utility in electron spectroscopy across the temperature range 100 °C to 20 °C using a laboratory ^{63}Ni radioisotope β^- particle source (end point energy = 66 keV). Monte Carlo simulations using the computer program CASINO were conducted and showed that the spectrometer had a quantum detection efficiency which increased with increasing electron energy up to 70 keV; a quantum detection efficiency of 73 % was calculated. The accumulated ^{63}Ni β^- particle spectra together with CASINO simulations of the detected spectra showed that the GaAs based spectrometer could be used for counting electrons and measuring the energy deposited per electron in the detector's active region (i layer). The development of a GaAs electron spectrometer of this type may find use in future space missions to environments of intense radiation (such as at the surface of Europa for investigation of electron-driven radiolysis of ice) and high temperature (such as at Mercury, and comets passing close to the Sun).

Key words: electron spectroscopy; semiconductor detector; Europa.

This article has been accepted for publication and undergone full peer review but has not been through the copyediting, typesetting, pagination and proofreading process which may lead to differences between this version and the Version of Record. Please cite this article as doi: 10.1029/2018JA025687

1 Introduction

This article reports characterisation of a prototype GaAs detector coupled to custom preamplifier electronics developed as part of efforts to realise a low-mass, low-volume, low-power, multi-mission capable direct-detection electron spectrometer that is tolerant of high temperatures (up to 100 °C) and extreme radiation. Such an instrument is anticipated to be of use in numerous future space missions. Electron spectrometers are commonly used to study interactions between the Solar wind and planetary atmospheres, magnetospheres, and surfaces (Livi et al., 2003). One promising use of electron spectroscopy is in the exploration of Jupiter's moon Europa.

A mission to Europa would particularly benefit from inclusion of an electron spectrometer given the dominance (both in terms of energy flux and particle number) of electrons (energies of 20 keV to 700 keV) over other ions in the radiation environment of Europa (Cooper at al., 2001). Understanding the Europan electron population and its interaction with the surface is profoundly important. Magnetometer measurements have indicated the existence of a liquid water ocean under Europa's water ice surface (Powell et al., 2005). The energy deposited by charge particles, predominately electrons, is thought to enable radiolytic processes to occur in the ice (Johnson et al., 2004). This likely radiolysis is thought to give rise to multiple compounds, such as SO_2 and CO_2, which have already been detected on the surface (Carlson, 2001; Lane et al., 1981). Furthermore, observations of Europa's surface have also revealed the presence of a hydrated compound, suggested to be hydrated sulfuric acid ($H_2SO_4{\cdot}nH_2O$) (Carlson et al., 1999) resulting from the bombardment of the icy surface with sulfur ions. However, it is important to note that because the electron population and indeed the wider radiation environment at Europa's surface is relatively poorly known, it is possible that at least some of the compounds present on the surface may originate from the ocean instead of, or as well as, radiolysis; an alternative interpretation of the observed hydrated compound at Europa's surface may be hydrated salt minerals or frozen brines ($MgSO_4$ and Na_2SO_4) whose presence may be explained by an extensive subsurface ocean containing dissolved salts being the source (McCord et al., 1999). Measurements of the electron population on the surface of Europa would enable the extent of the possible radiolytic contribution to the abundances of compounds including SO_2, CO_2, and hydrated compounds on the surface to be refined, with the implication that the relative contributions from radiolysis and transport from/to the ocean may be determined.

Provided an ocean-surface linkage exists (recent Europan auroral observations have been attributed to possible electron impact excitation of water vapour plumes; thus implying linkage between ocean and surface (Roth et al., 2014; Sparks et al., 2016)), an improved understanding of the radiolytic chemistry of the Europan surface may further enable properties of the ocean, such as its chemistry, to be determined. For example, if the abundances of the CO_2 and H_2 on the surface cannot be explained via radiolytic origin, transport of such material from hydrothermal vents to the surface is a likely source; the possibility that lithoautotrophic methanogenesis, the conversion of CO_2 and H_2 to methane, being a source of useful chemical energy for the production of biomass (McCollom, 1999), may then be further explored. Conversely, if the surface chemistry is found to be explainable as solely a product of the radiation and plasma environment's interaction with the surface ice, the species and abundances of such compounds on the surface may provide a useful proxy to understanding the extend and consequences of the transportation of oxidants and organics produced at the surface through the icy cell to the ocean via impact gardening (Phillips & Chyba, 2001). It should be noted here that in addition to endogenic materials (intrinsic to Europa) that are

subject to radiolysis at the surface of Europa, exogenic materials may also exist (such as materials of potential astrobiological interest delivered by comet impacts, and indeed material originating from other Jovian moons) (Johnson et al., 2004). Hence, understanding the radiolytic processes along with appropriate modelling, may help separate the endogenic and exogenic contributions. However, the intense radiation environment of Europa imposes limitations on the mission duration. The global average energy flux of electrons and ions with energies ranging from 10 keV to 200 MeV at Europa was estimated from modelling data from Voyager 1 and Galileo to be 5×10^{10} cm^{-2} s^{-1} keV^{-1} (Johnson et al., 2004; Paranicas et al., 2009). As such, Europa is considered one of the most challenging destinations for solar system exploration due to the intense radiation environment; radiation doses of 40 krad day^{-1} and 20 krad day^{-1} are expected for a Europa orbiter and lander, respectively (Kolawa et al., 2007).

The motivation to develop electron spectrometers for examination of radiolytic processes is not confined to science at Europa. Radiolytic processes occur also in the icy surfaces of asteroids and comets (Hudson & Moore, 1999). Deeper understanding of radiolysis on such bodies, which can be achieved with an electron spectrometer, could provide information about their processing and chemical evolution. Nor is the utility of an electron spectrometer confined to radiolytic science. Amongst the many other possible missions for an electron spectrometer of the type being developed, electron spectroscopy at Mercury deserves special mention due to the environmental demands that would be placed on the instrument. Mercury has a substantial internal magnetic field and a magnetosphere which hosts dynamical features with similarities to those that occur in Earth's magnetosphere (Domingue & Russell, 2007). Information regarding the nature and origin of Mercury's magnetic field and the determination of the structure of the planet's magnetic field would be provided through measurements of the electron population at Mercury, via orbiter and/or lander (Andrews et al., 2007). This can be achieved by electron energy and pitch angle measurements, within the energy range 15 keV to 300 keV.

The temperatures necessary to be endured by spacecraft at Mercury, and comets passing close to the Sun, can be extreme. For example, the temperature in polar locations on Mercury ranges between -50 °C to 70 °C (Novara, 2001). For comets, surface temperature measurements show great variation; as an example, they can range from -43 °C (67P/Churyumov–Gerasimenko at 3.5 AU (Fulle et al., 2016)) to 87 °C (Halley at 0.8 AU (Emerich et al., 1988)). The hotter temperatures in these environments make use of narrower bandgap semiconductor (e.g. Si) detectors impossible without cooling mechanisms, which increase the technological complexity, mass, cost, and volume of instruments based upon them. Wide bandgap semiconductors can overcome this challenge (Owens, 2012).

To date, a variety of electron spectrometers have been developed. For example, the Electron Spectrometer of the Cassini Plasma Spectrometer was a hemispherical top-hat electrostatic analyzer (ESA) with an annular microchannel plate (MCP) detector (Linder et al., 1998); MCP detectors require high voltages and high vacuums. Langmuir probes have also been frequently used (Gruenwald et al., 2013), but they are typically bulky. Indirect electron spectroscopy using scintillators with either photomultiplier tubes (Tatsuhiko et al., 2010) or photodiode detectors (Kriss & Hamby, 2004) to convert the scintillations into electrical signals is also a well-established technique. However, better energy resolution can be achieved with direct electron detection using semiconductor detectors due to the inefficiencies involved in the conversion of electrons to light with a scintillator (Knoll, 2010).

Direct electron detection has been investigated with semiconductor devices including solid state detectors (SSDs), charged coupled devices (CCDs), depleted p channel field effect transistors (DEPFETs), pixel detectors, and p^+-i-n^+ photodiodes. The Energetic Particle Spectrometer (EPS) on board the MESSENGER spacecraft, to Mercury (Andrews et al., 2007), the New Horizons Pluto Energetic Particle Spectrometer Science Investigation (PEPSSI) electron spectrometer (McNutt et al., 2008), and the Jupiter Energetic Particle Detector Instruments (JEDI) on board JUNO (Mauk et al., 2013), all used 500 μm thick ion-implanted Si SSDs electron detectors. CCDs have been studied for replacing MCP detectors in a collimator–electrostatic analyser head configuration, but they have been shown to be radiation damaged from high fluxes of energetic electrons (Bedington et al., 2012). Work has also been reported characterising Si DEPFETs for the detection of β^- particles from ^{3}H and ^{14}C β^- particle sources (Ulrici et al., 2005). Si hybrid pixel detectors (Bertolucci et al., 1996), Si monolithic active pixel detectors (Deptuch, 2005), and Si p^+-i-n^+ photodiodes (Vapirev et al., 1994), have all been investigated for electron detection. However, Si detectors suffer from high intrinsic carrier concentration at a given temperature due to their relative narrow bandgap (1.12 eV) (Neudeck et al., 2002). Si detectors can also suffer from radiation damage (Abbey et al., 2003) (Swinyard et al., 2009). As such, they commonly require cooling facilities and radiation shielding to help mitigate these limitations. However, wide bandgap semiconductor devices, such as GaAs, offer an alternative and may be used to eliminate or reduce the need for cooling and radiation shielding resulting in improvements in instrument lifetime and reductions in instrument mass, volume, power consumption, and complexity.

One of the favourable attributes of GaAs is its bandgap energy (1.42 eV at room temperature (Bertuccio & Maiocchi, 2002)) which results in a lower thermally generated leakage current density (and thus less parallel white noise (Lioliou & Barnett, 2015)) at a given temperature, compared to narrower bandgap semiconductors such as Si. The relatively low electron-hole pair creation energy of GaAs (4.184 eV at 300 K (Bertuccio & Maiocchi, 2002) provides similar charge carrier creation statistics and Fano-limited spectroscopic resolution as Si (Bertuccio, 2012). Furthermore, GaAs has been proven to be radiation resistance to γ-rays (Dixit et al., 2015; Ly Anh et al., 2006), fast neutrons (Ladzianský et al., 2009), and high energy electrons (Šagátová et al., 2014). Indeed, GaAs is more radiation hard than Si for γ-rays, electrons, and low energy protons and neutrons (Rossi et al., 2006). Thus, the use of a GaAs based electron spectrometer for space missions to high temperature and intense radiation environments may be beneficial.

Recently, GaAs p^+-i-n^+ mesa photodiodes with 10 μm thick i layers have been developed for photon counting X-ray spectroscopy. An X-ray energy resolution of 625 eV *FWHM* at 5.9 keV was measured with a 200 μm diameter device coupled to custom preamplifier electronics at room temperature (Lioliou & Barnett, 2016). Subsequent measurements showed that the GaAs detector spectrometer could operate uncooled at high temperatures (≥ 20 °C) for photon counting X-rays spectroscopy; a *FWHM* at 5.9 keV of 2.00 keV was measured with the detector and preamplifier both operating at 100 °C (Lioliou et al., 2017). Some preliminarily measurements were also made showing that the spectrometer was able to detect ^{63}Ni β^- particle particles at room temperature (Lioliou & Barnett, 2016) but the detector was not investigated fully for this purpose. Here, the suitability of an electron spectrometer employing a GaAs photodiode detector is characterised thoroughly for its high temperature performance. The electron spectrum predicted to be detected if the spectrometer was near Europa's orbit around Jupiter (9.5 R_J) is also considered, assuming that electrons were incident on the detector within the energy range 10 keV to 100 keV, after Paranicas et al. (2009).

2 Detector Structure

The detector used in the spectrometer was a custom GaAs p^+-i-n^+ mesa photodiode. It was grown and fabricated to the authors' specifications at the EPSRC National Centre for III-V Technologies, Sheffield, UK, on a commercial GaAs n^+ substrate by metalorganic vapour phase epitaxy (MOVPE). It had a p^+-i-n^+ structure with a 0.5 μm p^+ type GaAs layer, a 10 μm unintentionally doped i layer, and a 1 μm n^+ type GaAs layer. The doping density of both n^+ type and p^+ type layers was 2×10^{18} cm^{-3}. The photodiode had a diameter of 200 μm. It was chemically etched using a 1:1:1 H_3PO_4:H_2O_2:H_2O solution followed by 10 s in a 1:8:80 H_2SO_4:H_2O_2:H_2O solution. The top Ohmic contact consisted of 20 nm of Ti and 200 nm of Au. It covered 45 % of the surface of the device. The rear Ohmic contact consisted of 20 nm of InGe and 200 nm of Au. The GaAs device was unpassivated. The resulting wafer structure can be seen in Figure 1. The detector was mounted and wire bonded upon a TO-5 can.

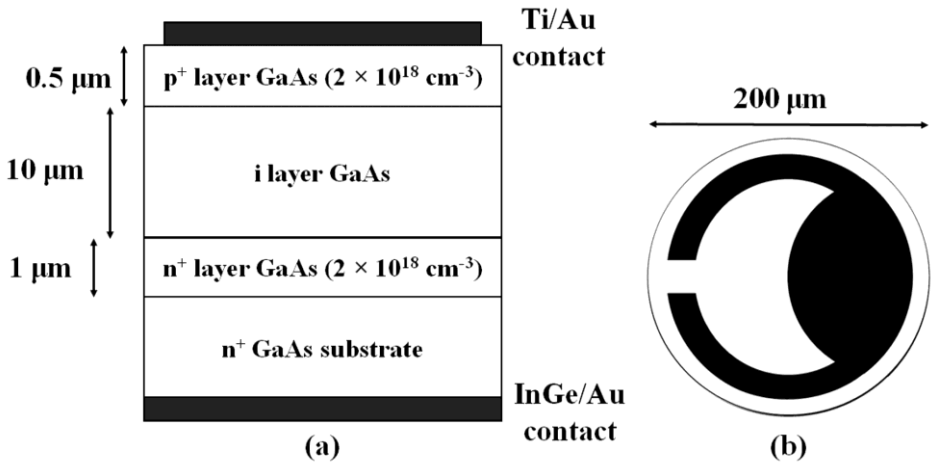

Figure 1. Illustrative (a) layers structure (not in scale) and (b) top-view of the GaAs p^+-i-n^+ photodiode.

3 Detector Electrical Characterization

The detector was electrically characterized within from a maximum temperature of 100 °C to a minimum temperature of 20 °C. Capacitance and dark current measurements as functions of applied reverse bias and temperature are presented below. The capacitance and the leakage current of the detector partially determine the energy resolution (*FWHM*) of the spectrometer (Lioliou & Barnett, 2015). Capacitance measurements allow the determination of the depletion width of the detector. Leakage current measurements as functions of temperature are also used to determine in part the likely temperature range that the spectrometer may function.

3.1 Capacitance Measurements

The capacitance was measured using an HP 4275A Multi Frequency LCR meter, with a 50 mV rms magnitude and a 1 MHz frequency test signal. The capacitance of the detector was measured as a function of applied reverse between temperatures of 100 °C and 20 °C. The detector was installed inside a TAS Micro MT climatic cabinet for temperature control; the temperature was initially set to 100 °C and then decreased to 20 °C, in 20 °C steps. To ensure thermal equilibrium, the detector was left to stabilize for 30 minutes at each temperature before the measurements were started. Dry N_2 was continually flowed into the climatic cabinet

throughout the measurements to maintain a dry (< 5% relative humidity) environment. The capacitance of the device's TO-5 package was also measured as a function of applied reverse bias and temperature and subtracted from the total measured capacitance of the packaged detector with the assumption that the capacitances acted in parallel. The total uncertainty of the determined detector capacitance was estimated to be ± 0.04 pF. It should be noted here that the reported detector capacitance variations with temperature form a single set of measurements taken at the same conditions (i.e. only the temperature was varied) and since no interconnections (cables etc.) were changed, the uncertainty associated with relative changes was estimated to be ± 0.005 pF (uncertainty associated with the HP 4275A Multi Frequency LCR meter). The measured capacitance of the detector with the capacitance of the package being subtracted, across the investigated temperature range can be seen in Figure 2.

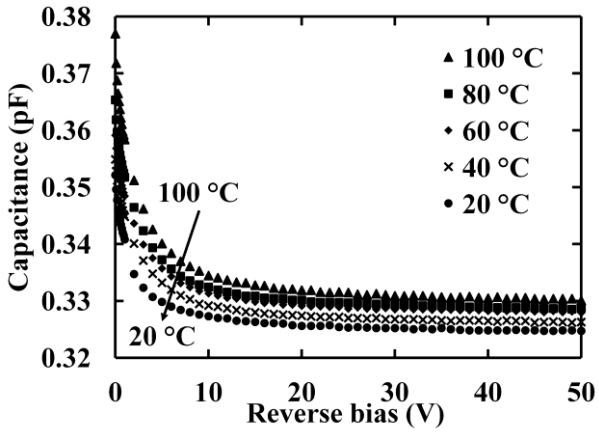

Figure 2. Measured capacitance of the GaAs p^+-i-n^+ mesa photodiode within the temperature range 100 °C to 20 °C.

The depletion layer capacitance, which defined the reverse biased diode capacitance, decreased from 0.377 pF ± 0.005 pF at 100 °C to 0.352 pF ± 0.005 pF at 20 °C at zero applied bias, and from 0.330 pF ± 0.005 pF at 100 °C to 0.325 pF ± 0.005 pF at 20 °C, at -50 V reverse bias. The most significant capacitance change with temperature occurred at low applied reverse bias, whereas the capacitance at -50 V reverse bias was found to not be a function of temperature, within uncertainties, for the investigated temperature range.

The measured depletion layer capacitance was used to calculate the depletion layer width (Sze & Ng 2007) as a function of applied reverse bias and temperature, and can be seen in Figure 3 for the maximum and the minimum investigated temperatures. The depletion layer width was found to increase from 9.5 μm ± 0.1 μm at 100 °C to 10.2 μm ± 0.1 μm at 20 °C at zero applied bias. At applied reverse biases (magnitude) > -6 V, the depletion layer width was found to be temperature independent, within uncertainties, for the investigated temperature range. The temperature dependence of the depletion layer width at low reverse biases was attributed to the possible presence of a thin region around the depletion layer with non-ionized dopants at low temperatures, which were progressively ionized at high temperatures thus limiting the extension of the depletion layer (Mazzillo et al., 2012). For highly doped p^+ and n^+ regions (such as 2×10^{18} cm^{-3} for the currently reported photodiode), the maximum depletion layer is set by the i layer thickness. Thus, it can be said that the i layer thickness of the GaAs p^+-i-n^+ mesa photodiode was found to be 11 μm ± 1 μm.

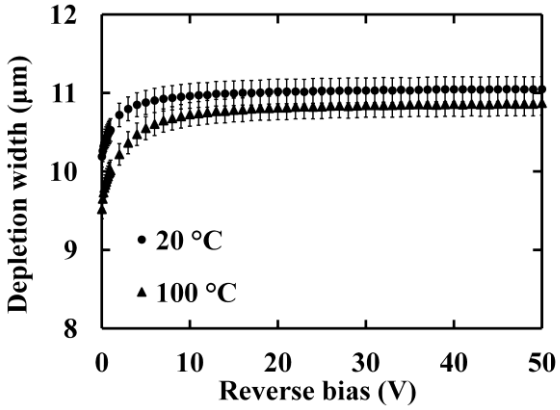

Figure 3. Calculated depletion width of the GaAs p^+-i-n^+ mesa photodiode at 100 °C (filled triangles) and 20 °C (filled circles).

3.2 Current Measurements

The current was measured using a Keithley 6487 Picoammeter/Voltage Source. The detector was installed inside a TAS Micro MT climatic cabinet for temperature control, as per the capacitance measurements. The leakage current associated with the detector's TO-5 can was also measured as a function of bias and temperature.

The measured leakage current of the detector, with the leakage current of the package subtracted, as a function of applied reverse bias and temperature can be seen in Figure 4. The leakage current at -5 V applied reverse bias (the normal operating bias of the detector and that used in spectroscopic measurements reported in section 5) was found to decrease from 1.171 nA ± 0.006 nA (3.73 μA cm^{-2} ± 0.02 μA cm^{-2}) at 100 °C, to 1.3 pA ± 0.4 pA (4 nA cm^{-2} ± 1 nA cm^{-2}) at 20 °C. Similarly, the leakage current at the maximum investigated reverse bias, -50 V (corresponding to an internal electric field of 50 kV cm^{-1}),was found to decrease from 1.684 nA ± 0.007 nA (5.36 μA cm^{-2} ± 0.02 μA cm^{-2}) at 100 °C, to 1.7 pA ± 0.4 pA (6 nA cm^{-2} ± 1 nA cm^{-2}) at 20 °C. A previously reported 10 μm GaAs mesa p^+-i-n^+ photodiode (200 μm diameter) had a leakage current density of 5.14 μA cm^{-2} at 100 °C and 50 kV cm^{-1} internal electric field (Lioliou et al., 2017). A previously reported thinner (7 μm) GaAs mesa p^+-i-n^+ photodiode (200 μm diameter) had a leakage current density of 2 μA cm^{-2} at 100 °C and 21.4 kV cm^{-1} internal electric field (Lioliou et al., 2016). Another different GaAs pixel p-i-n mesa photodiode detector has been previously reported with a leakage current density of 92 nA cm^{-2}, at 30 °C and 33 kV cm^{-1} applied electric field (Bertuccio et al., 2003).

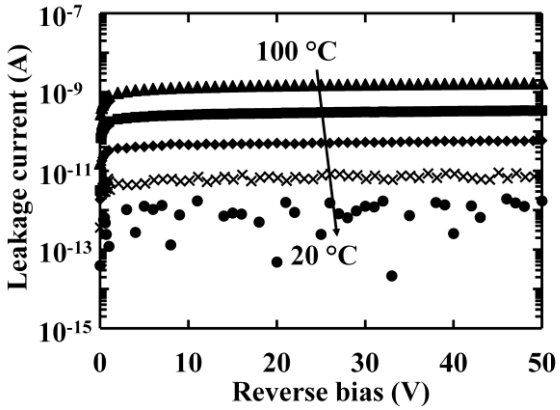

Figure 4. Leakage current as a function of applied reverse bias of the GaAs p^+-i-n^+ mesa photodiode in the temperature range 100 °C down to 20 °C.

4 Quantum Detection Efficiency of the Detector

The computer program CASINO (Drouin et al., 1997; Hovington et al., 1997) was used to predict the detector's quantum detection efficiency, *QE*, for each energy of electron (ratio between the total electron energy deposited in the active layer and the total electron energy incident on detector's face). At each energy, from 1 keV to 100 keV in 1 keV steps, 4000 electrons were simulated at each energy as incident on a portion of the detector's face which was covered by the detector's top contact. A second set of simulations, with the same characteristics, was simulated as incident on a portion of the detector's face which was not covered by the detector's top contact. The results of the simulations were then combined in appropriate proportions to account for the proportions of the detector's face that were covered with the contact (45%) and not covered with the contact (55%). In each case, the p^+ layer, n^+ layer, and substrate of the detector were considered to be entirely inactive; i.e. any electron energy absorbed in these regions did not usefully contribute to the quantum efficiency. The quantum efficiency predicted from these simulations is presented in Figure 5.

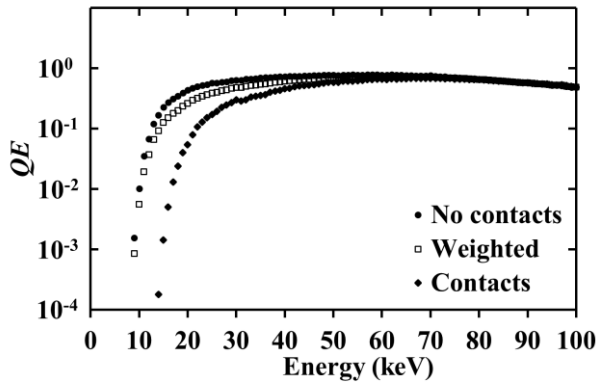

Figure 5. Quantum detection efficiency, *QE*, of the detector for electrons of each energy, in detector regions covered by top contacts (diamonds) and not covered by top contacts (circles) as a function of incident electron energy. The weighted quantum efficiency is also shown (open squares).

The quantum detection efficiency of the detector remained < 0.0001 for electrons of energy up to 8 keV when they were incident on the optical window of the detector and up to 13 keV when they were incident on the detector's Au/Ti top Ohmic contact. For both simulated cases (with and without top contacts), the quantum detection efficiency increased with increasing electron energy, up to 60 keV when electrons were incident on the optical window of the detector and up to 66 keV when electrons were incident on the Au/Ti top Ohmic contact. The absorption of electrons at low energies was limited by the absorption of electrons in the top layers (top Ohmic contacts and/or p^+ layer). At high electron energies, > 62 keV for electrons incident optical window of the detector and > 70 keV when they were incident on the detector's top contact, electrons were also absorbed at the n^+ layer/substrate, thus explaining the decrease of the quantum efficiency. The weighed quantum efficiency (i.e. assuming uniform illumination of the detector, thus including illumination of both the contact and optical window) reached a value of 73% at 59 keV, and remained stable up to 70 keV, suggesting that the thickness of the i layer (10 μm) did not limit the absorption of electrons at the ^{63}Ni endpoint energy (66 keV). However, the weighted quantum efficiency decreased at electron energies > 70 keV, and

reached a value of 49% at 100 keV. A thicker i layer would be required for the optimal absorption of electrons with energies greater than 70 keV; it was found that 35 μm and 105 μm of GaAs would fully absorb electrons with energies up to 100 keV and 200 keV, respectively. It is possible that the eventual electron spectrometer for the proposed uses would actually consist of two channels with separate detectors possibly made of different materials; one channel optimised for softer (e.g. 10 keV – 100 keV) electrons and one optimised for harder electrons (e.g. energy > 100 keV), in order to maximise spectrometer performance across the entire energy range.

5 Expected and Experimental Measurements of ^{63}Ni β^- Particle Spectra

The high temperature performance of the electron spectrometer employing a GaAs photodiode detector was investigated using a ^{63}Ni radioisotope β^- particle source. The ^{63}Ni radioisotope β^- particle source was a 7 mm × 7 mm foil with a protective Ni overlayer (~1 μm) covering the ^{63}Ni radioisotope β^- particle source. The actual activity of the ^{63}Ni radioisotope β^- particle source was 185 MBq. The apparent activity of the ^{63}Ni radioisotope β^- particle source, due to self-absorption within the source (Alam & Pierson, 2016), was calculated to be 136 MBq.

5.1 Expected Spectrum Incident on the Detector

In order to identify the different losses and aid the development of the electron spectrometer presented here, the spectrum emitted by the ^{63}Ni radioisotope β^- particle source and its absorption before reaching the detector was simulated using the computer program CASINO (Drouin et al., 1997; Hovington et al., 1997;). The β^- particles, after their emission from the ^{63}Ni radioisotope β^- particle source and before reaching the top face of the detector, may deposit energy in the protective Ni overlayer (~1 μm) covering the ^{63}Ni radioisotope β^- particle source and the N_2 layer (3.2 mm) between the ^{63}Ni radioisotope β^- particle source and the top of the detector. The result of these simulations was the calculation of the spectrum incident on the detector.

The simulated electrons had energies from 1 keV to 66 keV (the ^{63}Ni endpoint energy), with a step of 1 keV; different numbers of electrons were simulated for each energy to reflect the different emission probability, P_i, of each β^- particle energy including the effects of self-absorption in the source (Liu et al., 2015). A total of 18,361,685 electrons were simulated using a bank of 14 computers each with an Intel i7-6700, 4 cores, 3.40 GHz processor and 32 GB of random access memory. The inactive Ni overlayer (thickness of 1 μm and density of 8.908 g cm^{-3}) and the N_2 layer (thickness of 3.2 mm and density of 0.0012 g cm^{-3}) were included in the simulations. CASINO was configured to perform the simulations using its Mott by Interpolation model. The authors of CASINO have previously reported this configuration to be faster than using empirical forms of the Mott cross section, to be more accurate than using analytical fits, and to require less computation time than use of the Rutherford cross section (Drouin et al., 1997). In CASINO the Ionisation Potential was set as per Joy & Luo (1989). The Random Number Generator was of Press et al. (1986). The Directing Cosine was specified as Hovington et al. (1997). The Effective Section Ionisation was selected to be Casnati et al. (1982). The computed trajectories of all electrons simulated were used to calculate their total remaining energy after passing through the Ni overlayer and N_2 layer. The distribution of particle energy remaining for electrons of each energy simulated, was considered, and the distributions for all energies summed, thus resulting in the spectrum predicted to be incident on the detector from the ^{63}Ni radioisotope β^- particle source. This can be seen in Figure 6.

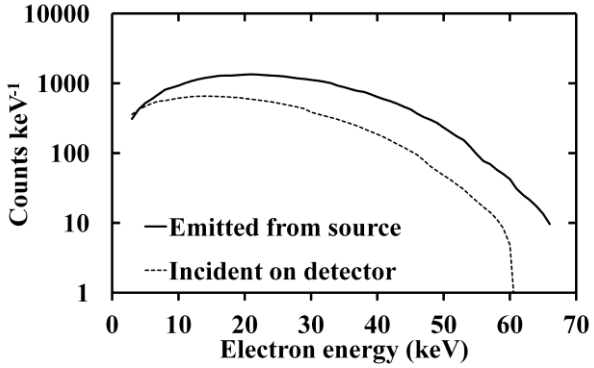

Figure 6. Simulated ^{63}Ni β^- particle spectrum as emitted from the source (solid line), and incident on the top face of the detector (square dots).

5.2 Experimentally Measured and Expected Detected ^{63}Ni β^- Particle Spectrum

The detector (packaged in a TO-5 can) was connected to custom-made low-noise charge-sensitive preamplifier of feedback resistorless design of similar to that reported in ref. (Bertuccio et al., 1993). The output signal of the preamplifier was shaped using an Ortec 572A shaping amplifier which was further connected to a multi-channel analyser (MCA) for digitisation. This prototype electron spectrometer was then characterised with the detector and preamplifier at temperatures between 100 °C and 20 °C, in 20 °C steps. The detector and preamplifier were placed inside a climatic cabinet as per the electrical characterisation measurements reported above.

Initially, an ^{55}Fe radioisotope X-ray source (Mn Kα at 5.9 keV and Mn Kβ at 6.49 keV (Schötzig, 2000)) was used to illuminate the detector at each temperature. This enabled the charge scale of the spectrometer to be energy calibrated based on the positions of the zero energy noise peak and Mn Kα peak. The ^{55}Fe X-ray spectra allowed the identification of the optimum reverse bias and shaping time for the spectrometer at each temperature to give the best energy resolution. The optimum reverse bias was found to be -5 V within the investigated temperature range. The optimum shaping time to give the best energy resolution, as quantified by the Full Width at Half Maximum (*FWHM*) at 5.9 keV, was found to lengthen with decreasing temperature; it was found to be 0.5 μs at 100 °C, 80 °C, and 60 °C, 1 μs at 40 °C, and 2 μs at 20 °C. The optimum shaping time is achieved when the summation (in quadrature) of the shaping time varied noise contributions, i.e. parallel white noise (leakage current dependent) and series white noise (capacitance dependent) is minimized (Lioliou et al., 2017). The presently reported spectrometer had a more significant reduction in leakage current than in capacitance as the temperature decreased, explaining the lengthening of the optimum shaping time with decreased temperature. The energy resolution (*FWHM*) at 5.9 keV was found to be 0.65 keV at 20 °C, and 1.95 keV at 100 °C.

Following this, the ^{55}Fe radioisotope X-ray source was removed and a ^{63}Ni radioisotope β^- particle source (66 keV endpoint energy) was positioned 3.2 mm above the top of the detector. The block diagram of the spectra accumulation set up can be seen in Figure 7. Spectra were again collected as a function of temperature (100 °C to 20 °C), with the detector reverse biased at -5V, and with the shaping time set as determined to be best at each temperature previously. The live time limit for each accumulated spectrum was 900 s. A low energy threshold was set to minimize counts from the zero energy noise peak.

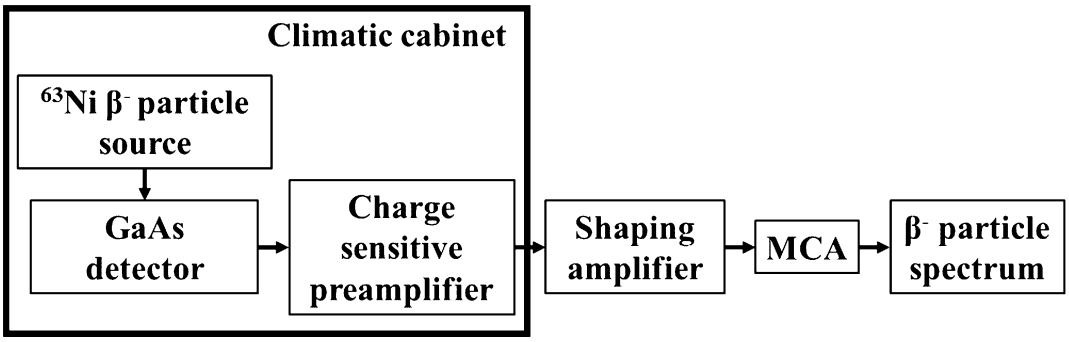

Figure 7. Block diagram of the spectra accumulation set up.

Since changing the shaping time had the effect of changing the effective channel width (in units of eV) of MCA as would be expected, the accumulated spectra were recalibrated so that they could be presented in terms of counts per 1 keV thus enabling comparisons. The accumulated electron spectra presented in this way can be seen in Figure 8.

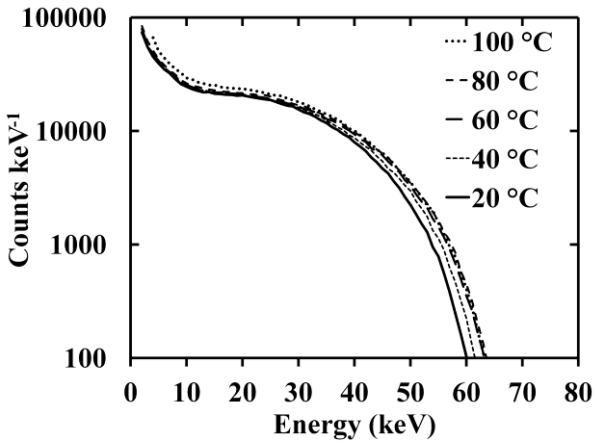

Figure 8. Experimentally measured ^{63}Ni β$^-$ particle spectra (counts per 1 keV as a function of energy) within the investigated temperature range (between 100 °C and 20 °C, with 20 °C decrements).

The apparent endpoint energy measured with the GaAs based electron spectrometer was 60 keV at 20 °C. The apparent endpoint energy was found to be 61 keV at 40 °C, and 63 keV at 60 °C, 80 °C, and 100 °C. The variation of the endpoint energy with temperature may be partially attributed to the different energy resolution (*FWHM*) of the spectrometer at different temperatures. Also, due to the increase of the Fano noise with increasing energy (Bertuccio, 2012), the energy resolution was expected to worsen slightly at 60 keV compared with that measured at 5.9 keV; a *FWHM* at 60 keV of 0.76 keV and 1.99 keV at 20 °C and 100 °C, respectively, was calculated assuming a Fano factor of 0.12 (Bertuccio et al., 1997) and considering the electronic noise components of the spectrometer in addition to the Fano noise. The dependency of the electron hole pair creation energy, ε, with temperature within the investigated temperature range was also considered; the linear dependency found by Bertuccio & Maiocchi (2002) of ε [eV] = 4.55 – 0.00122T [K] within the temperature range 230 K to 320 K was extrapolated to cover the investigated temperature range.

CASINO simulations were then used to investigate and explain the difference between the ^{63}Ni radioisotope β$^-$ particle source endpoint energy (66 keV), and the apparent endpoint energy of the accumulated spectrum at 20 °C shown in Figure 8.

Having computed the electron (β^- particle) spectrum incident on the detector (Figure 6, section 5.1), the spectrum of electrons expected to be usefully absorbed by the detector was then calculated considering the computed quantum efficiency of the detector (Figure 5, section 4), thus taking to account energy losses within the dead layers of the detector (considered to be the top Ohmic contact covering 45% of the detector face, the p^+ layer, the n^+ layer, and the substrate). The resulting spectrum was the electron energy spectrum predicted to be detected from absorption of β^- particles in the active i layer of the detector, but without any Fano or spectrometer electronic noise considered. The detected spectrum resulting from the CASINO simulations was then normalized to reflect the number of β^- particles emitted by the ^{63}Ni radioisotope β^- particle source during the accumulation of the spectrum (live time of 900 s). Figure 9 shows the accumulated ^{63}Ni β^- particle spectrum at 20 °C, along with the expected incident on the detector spectrum, and expected detected spectrum.

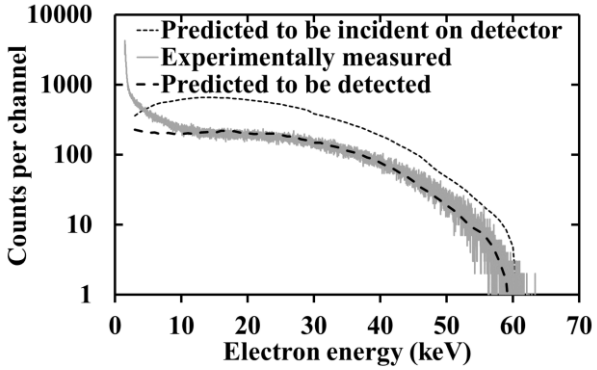

Figure 9. Comparison between the accumulated ^{63}Ni β^- particle spectrum at 20 °C (grey solid line) and the predicted to be detected spectrum (black dashes). The spectrum incident on the detector as calculated with CASINO simulations is also shown.

5.3 Discussion

The difference between the ^{63}Ni β^- particle spectrum emitted from the source and the accumulated spectrum were explained using the results from the CASINO simulations (sections ***5.1 Expected Spectrum Incident on the Detector*** and ***5.2 Experimentally Measured and Expected Detected ^{63}Ni β^- Particle Spectrum)***: electrons (β^- particles) lose energy along their path through matter, hence the total energy deposited by each β^- particle in the active layer of the detector is different from its initial energy, and it depends upon its initial energy and track from the ^{63}Ni radioisotope β^- particle source to the active layer of the detector. Electron (β^- particle) energy losses within the Ni overlayer, the N_2 layer, the top contact, the p^+ layer, as well as the n^+ layer/substrate explained the difference between the emitted from the source and the accumulated ^{63}Ni β^- particle spectrum. The expected detected spectrum was in a good agreement with the accumulated ^{63}Ni β^- particle spectrum at 20 °C (see Figure 9) at energies $\geq$ 10 keV. At low energies, < 10 keV, the discrepancy between the simulated detected spectrum and the accumulated ^{63}Ni β^- particle spectrum is currently unknown with absolute certainty. The right hand side of the spectrometer zero energy peak tail not being entirely eliminated with the low energy threshold of 2 keV (the same energy threshold entirely eliminated the zero energy peak tail of the ^{55}Fe X-ray spectrum at 20 °C) as a result of increased stray capacitive load on the input of the preamplifier due to the mechanical package of the ^{63}Ni radioisotope β^- particle source being different compared to that of the ^{55}Fe radioisotope X-ray source, could explain the increased number of counts in the accumulated ^{63}Ni β^- particle spectrum compared

to the simulated detected spectrum. Similar effects in a GaAs based β^- particle spectrometer measuring a ^{14}C radioisotope β^- particle source were attributed to this phenomenon (Barnett et al., 2012). However, the presence of the mechanical package of the ^{63}Ni radioisotope β^- particle source in the reported set up is expected to have negligible capacitive effects.

For developmental purposes, accurately predicting the detected spectrum, given that the incident electron spectrum is known, is essential for quantitative analysis of the accumulated electron spectra. When such a spectrometer is used for its intended application, the inverse is true: the incident spectrum would be reconstructed from the detected spectrum. The energy deposited in the active region of the detector does not equal the energy of the incident electron, but is only statistically related to the energy of the incident electron (Vampola, 1998). Thus understanding processes such as electron energy deposition, scattering, and backscattering within the electron spectrometer (and any future instrument optics) is necessary for extracting information from the accumulated electron spectra and identifying the original electron spectra incident on the instrument.

As shown in Figure 9, the GaAs detector coupled to the readout electronics can be used for counting β^- particles and measuring the total energy per particle deposited in the detectors active region (i layer). Reducing the total area of the detector face covered by the top Ohmic contact and reducing the thickness of the p^+ layer, within practicalities, would minimize the losses of electron energies at the top dead layers, allowing the more complete absorption of the energy of each electron incident on the detector. The thickness of the p^+ layer may be possibly reduced by etching of the p^+ layer in the region not covered by the top Ohmic contact. The thickness of the active layer of the detector (10 μm i layer), did not limit the absorption of high electron energies (up to 66 keV) (Figure 5), however, the efficient absorption of electrons with energy > 66 keV electrons would require a thicker active layer. Increasing the thickness of the i layer to e.g. 35 μm or 105 μm would allow full absorption of electrons up to 100 keV or 200 keV, respectively.

The reported GaAs based electron spectrometer has been demonstrated to function up to 100 °C (Figure 8), within the energy range 1 keV to 66 keV. Previous reports on GaAs have proved the material's high radiation resistance (eg. Dixit et al. (2015) ; Ladzianský et al. (2009); Ly Anh et al. (2006); Rossi et al. (2006) and Šagátová et al. (2014)). Both of these attributes suggest that the reported electron spectrometer may be used in numerous future space missions to intense radiation and high temperature environments (up to 100 °C, without the need for cooling). Thus direct detection electron spectroscopy with a simpler instrument thermal management system and reduced instrument radiation shielding compared to that required for a traditional Si electron detector may be achieved. This is beneficial for electron spectroscopy in environments where these attributes are desirable or required, for example, for the examination of radiolytic processes occurring at surfaces of Europa and comets, and determination of the nature and origin of the magnetic field of Mercury.

Since the accumulated spectrum and the spectrum expected to be detected by the spectrometer were in good agreement for the ^{63}Ni radioisotope β^- particle source, the response of the reported electron spectrometer in the environment of Europa was considered. The omnidirectional electron flux computed by Paranicas et al. (Paranicas et al., 2009) based on the Divine and Garrett model, and Voyager 1 and Galileo data, at a radial distance of 9.5 R_J, near Europa's orbit, was used to represent Europa's radiation environment, and can be seen in Figure 10. For clarity, only the softer (e.g. 10 keV – 100 keV) electrons were included in the prediction of the

electron spectrometer response in Europa, given the quantum detection efficiency of the spectrometer (Figure 5, section 4).

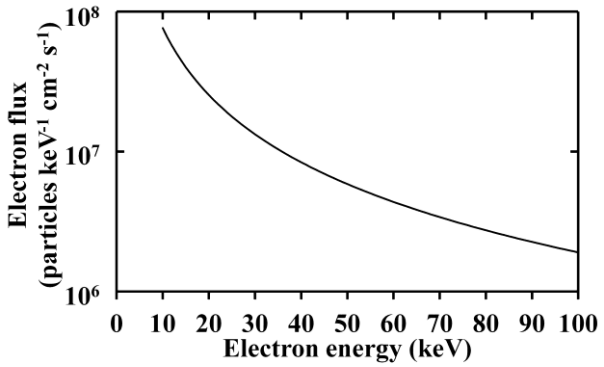

Figure 10. Omnidirectional electron flux expected at Europa (9.5 R_J) as a function of energy, after Paranicas et al. (2009).

The electron spectrum incident on the detector was then computed: the electron flux at Europa (Figure 10) was divided by 2 (assuming the detector is single sided) and multiplied by the area of the detector (3.14×10^{-4} cm^2). Having computed the electron spectrum incident on the detector (counts keV^{-1} s^{-1}), the spectrum of electrons expected to be usefully absorbed by the detector was calculated. Energy losses within the dead layers of the detector (the top Ohmic contact covering 45% of the detector face, the p^+ layer, the n^+ layer, and the substrate) were taken to account, in order to predict the detected spectrum from absorption of electrons in the active i layer of the detector, at Europa. This was achieved by considering the computed quantum efficiency of the detector (Figure 5, section 4). The spectra predicted to be incident on the detector and to be detected can be seen in Figure 11. It should be noted here that the Fano noise and the spectrometer's electronic noise were excluded from the predictions. Given that the response of the spectrometer is well-known (the match between the expected and experimentally measured ^{63}Ni β^- spectra is good) for a real detected spectrum accumulated at Europa, it would be possible to transform the spectrum detected into the spectrum incident on the detector and thus determine the energy characteristics of the electron population at Europa. Similar can be said for other applications such as measurements of electron populations at Mercury and near Sun comets, where the spectrometer could operate uncooled at temperatures ≤ 100 °C.

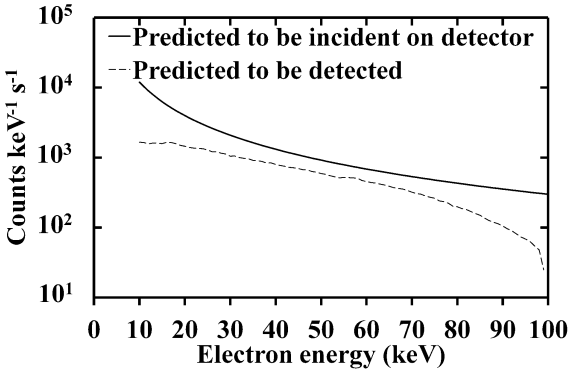

Figure 11. Comparison between the predicted to be incident on detector (solid line) and to be detected (black dashes) electron spectra (10 keV to 100 keV) of the radiation environment near Europa's orbit. Electron energy losses within the top contact, the p^+ layer, and the n^+

layer/substrate explained the difference between the spectra predicted to be incident and predicted to be detected.

Predicting the likely detected electron spectra (counts keV^{-1} s^{-1}) in a specific application allows the required accumulation times to be considered. In order to accurately identify the incident electron spectrum from the detected spectrum, the statistics need to be good (Vampola, 1998); Figure 11 suggests that an accumulation time of the order ~10 s per spectrum will be sufficient across this energy range if the Paranicas et al. (2009) data represents the reality at Europa.

Ignoring data storage and transmission limitations, and assuming negligible dead time in the spectra accumulation, the shortest (best resolution) spatial sampling distance can be estimated for an electron spectrometer of this type in orbit around Europa. For a spacecraft in orbit around Europa at an altitude of ~100 km with zero eccentricity (assuming a Europa radius of 1560.8 km and a Europa gravitational parameter of 3201 km^3 s^{-2} (Paskowitz & Scheeres, 2006)), the spacecraft would travel 13.8 km in 10 s, hence 759 spectra could be accumulated per orbit with a ≈ 14 km spatial resolution.

In order to refine the possible radiolytic contribution and/or ocean origin of the compound abundances revealed to be present on Europa, such as hydrated compounds, the correlation between the spatial distribution of the compounds and the spatial distribution of electrons should be investigated. Spectral images (reflectance spectra) from the Galileo Near Infrared Mapping spectrometer, NIMS, were previously used to map the hydrated compound distribution on Europa (Carlson et al., 2005). A strong asymmetry was found between the leading and trailing hemisphere of Europa for the hydrate content. A similar asymmetry was also suggested for the electron distribution based on calculations of the electron deposition on Europa's surface (Paranicas et al., 2001; Paranicas et al., 2009). A spatial resolution for the electron spectrometer similar to or better than the variation in the spatial distribution of the compounds of interest on the surface would be desirable in order to resolve electron spectra spatial variations and correlate them with the abundances of the surface compounds. The spatial resolution of NIMS was between 7 km and 39 km when global mapping was performed and 1.7 km when regional mapping was constructed (Carlson et al., 2005). The spatial resolution of the reported electron spectrometer could be improved by using a larger area detector. As examples, the spectrum accumulation time could be halved (thus resulting in a spatial resolution ≈ 7 km whilst maintaining the same statistics) if a GaAs detector with a 282 μm diameter was used; a GaAs detector with a 550 μm diameter would provide a spatial resolution of ≈ 2 km and thus provide similar spatial resolution mapping of the electron population in orbit, as the NIMS regional mapping of compounds on the surface.

Looking even further to the future of Europan radiolytic science, measurements by an electron spectrometer of this type either on or close to the surface (deployed for example on one or more landers, rovers, or aerobots) would enable the ground truth electron environment to be established and related to orbiter measurements. Measurements by an electron spectrometer on one or more penetrators would enable the surface and subsurface radiation environments to be measured. These experiments coupled with further terrestrial laboratory investigations of how electrons process simulant Europa-style ices would enable substantially better models of Europa's surface chemistry, and possibly even sub-surface and ocean chemistry, to be created.

6 Conclusions

Work towards the development of a multi-mission capable direct detection electron spectrometer suitable for use in harsh space environments has been reported. Development of such a multi-mission capable instrument would enable technology reuse and hence space missions with reduced costs and risks. One use of such an instrument would be to quantify the electron environment at Europa as part of efforts to understand the electron-driven radiolytic processes taken place on its surface.

As part of this, an electron spectrometer employing a GaAs p^+-i-n^+ circular mesa photodiode detector (200 μm diameter) and a custom-made charge-sensitive preamplifier was investigated at temperatures up to 100 °C. The detector was initially electrically characterized as a function of temperature, and the spectrometer was then characterized using simulations and laboratory measurements with a ^{63}Ni radioisotope β^- particle source.

The quantum efficiency of the instrument and the spectra expected to be detected by the instrument during the measurements were calculated using the computer program CASINO. Good agreement was found between the spectra predicted from the simulations and those obtained during the experiments, thus giving confidence that the performance of the instrument was well-understood. It was also experimentally shown that the spectrometer could detect electrons spectroscopically from the ^{63}Ni radioisotope β^- particle source across this temperature range.

The electron spectrum predicted to be detected by such an instrument near Europa's orbit (9.5 R_J) was considered, accounting for electrons incident on the detector with energies up to 100 keV. Given the expected electron fluences, such an instrument could provide a new spectrum for every ~14 km travelled in orbit around Europa. Use of a larger area detector would proportionally improve (shorten) the distance travelled during each spectrum accumulation, and thus further improve the spatial resolution obtained. Measurements of this type have value in investigating the radiolytically produced chemistry of Europa's surface where many compounds (detected via the Galileo Near Infrared Mapping spectrometer) are thought to be of radiolytic origin.

Acknowledgements

This work was in part supported by the Science and Technology Facilities Council, United Kingdom, through grants ST/M004635/1 and ST/P001815/1 (A.M.B., PI). A.M.B. acknowledges funding from the Leverhulme Trust, United Kingdom, in the form of a 2016 Philip Leverhulme Prize. M.D.C.W. acknowledges funding received in the form of Ph.D. scholarships from the University of Sussex, UK. The authors are grateful to B. Harrison, R.J. Airey, and S. Kumar at the EPSRC National Centre for III-V Technologies for material growth and device fabrication.

Data availability

Data are available from http://dx.doi.org/10.25377/sussex.6899954.

References

Abbey, A.F., Bennie, P.J., Turner, M.J.L., Altieri, B., & Rives, S., (2003). Cooling out the radiation damage on the XMM-Newton EPIC MOS CCDs. *Nuclear Instruments and Methods in Physics Research A, 513*, 136-142.

Alam, T.R., & Pierson, M.A., (2016). Principles of betavoltaic battery design. *Journal of Energy, 3*, 11-41.

Andrews, G.B., Zurbuchen, T.H., Mauk, B.H., Malcom, H., Fisk, L.A., Gloeckler, et al., (2007). The energetic particle and plasma spectrometer instrument on the MESSENGER spacecraft. *Space Science Reviews, 131*, 523-556.

Barnett, A.M., Lees, J.E., & Bassford, D.J., (2012). Direct detection of Tritium and Carbon-14 beta particles with GaAs photodiodes. *Journal of Instrumentation, 7*, P09012.

Bedington, R., Kataria, D., & Walton, D., (2012). Using a CCD for the direct detection of electrons in a low energy space plasma spectrometer. *Journal of Instrumentation*, 7, C01079.

Bertolucci, E., Conti, M., Grossi, G., Mancini, E., Russo, P., Campbell, M., et al., (1996), Use of silicon and GaAs pixel detectors for digital autoradiography. Paper presented at IEEE Nuclear Science Symposium, Anaheim, CA.

Bertuccio, G., (2012). The silence of the amps: integrated circuits for very-low-noise processing of random signals from radiation detectors. *IEEE Solid-State Circuits Magazine, 4*, 36-45.

Bertuccio, G., Casiraghi, R., Maiocchi, D., Owens, A., Bavdaz, M., Peacock, A., et al., (2003). Noise analysis of gallium arsenide pixel X-ray detectors coupled to ultra-low noise electronics. *IEEE Transactions on Nuclear Science, 50*, 723-728.

Bertuccio, G. & Maiocchi, D., (2002). Electron-hole pair generation energy in gallium arsenide by x and γ photons. *Journal of Applied Physics, 92*, 1248-1255.

Bertuccio, G., Pullia, A., Lauter, J., Forster, A., & Luth, H., (1997). Pixel X-ray detectors in epitaxial gallium arsenide with high-energy resolution capabilities (Fano factor experimental determination). *IEEE Transactions on Nuclear Science, 44*, 1-5.

Bertuccio, G., Rehak, P., & Xi, D., (1993). A novel charge sensitive preamplifier without the feedback resistor. *Nuclear Instruments and Methods in Physics Research A, 326*, 71-76.

Carlson, R.W., (2001). Spatial distribution of carbon dioxide. Hydrogen peroxide, and sulfuric acid on Europa, *Bulletin of the American Astronomical Society, 33*, 1125.

Carlson, R.W., Anderson, M.S., Mehlman, R., & Johnson, R.E., (2005). Distribution of hydrate on Europa: further evidence for sulfuric acid hydrate. *Icarus, 177*, 461-471.

Carlson, R.W., Johnson, R.E., & Anderson, M.S., (1999). Sulfuric acid on Europa and the radiolytic sulfur cycle. *Science, 286*, 97-99.

Casnati, E., Tartari, A., & Baraldi, C., (1982). An empirical approach to K-shell ionisation cross section by electrons. *Journal of Physics B: Atomic and Molecular Phusics*, 15, 155-167.

Cooper, J.F., Johnson, R.E., Mauk, B.H., Garrett, H.B., & Gehrels, N., (2001). Energic ion and electron irradiation of the icy Galilean satellites. *Icarus, 149*, 133-159.

Deptuch, G., (2005). Tritium Autoradiography with thinned and back-side illuminated monolithic active pixel sensor device. *Nuclear Instruments and Methods in Physics Research A, 543*, 537-548.

Dixit, V.K., Khamari, S.K., Manwani, S., Porwal, S., Alexander, K., Sharma, et al., (2015). Effect of high dose γ-ray irradiation on GaAs p-i-n photodetectors. *Nuclear Instruments and Methods in Physics Research A, 785*, 93-98.

Drouin, D., Hovington, P., & Gauvin, R., (1997). CASINO: A new Monte Carlo code in C language for electron beam interactions—part II: tabulated values of the Mott Cross section. *Scanning*, 19, 20-28.

Emerich, C., Lamarre, J.M., Moroz, V.I., Combes, M., Sanko, N.F., Nikolsky, Y.V., et al., (1988), *Temperature and size of the nucleus of comet P/Halley deduced from IKS infrared Vega 1 measurements*, in M. Grewing, R Praderie, R. Reinhard (Eds.), *Exploration of Halley's comet* (p. 839), Berlin, Germany: Springer – Verlag.

Fulle, M., Altobelli, N., Buratti, B., Choukroun, M., Fulchignoni, M., Grün, E., et al., (2016). Unexpected and significant findings in comet 67P/Churyumov–Gerasimenko: an interdisciplinary view. *Monthly Notices of the Royal Astronomical Society, 462*, S2-S8.

Gruenwald, J., Tskhakaya, D., Kovačič, J., Čerček, M., Gyergyek, T., Ionita, C., & Schrittwieser, R., (2013). Comparison of measured and simulated electron energy distribution functions in low-pressure helium plasmas. *Plasma Sources Science and Technology, 22*, 015023.

Hovington, P., Drouin, D., & Gauvin, R., (1997). CASINO: A new Monte Carlo code in C language for electron beam interaction —part I: Description of the program. *Scanning, 19*, 1-14.

Hudson, R.L., & Moore, M.H., (1999). Laboratory studies of the formation of methanol and other organic molecules by water + carbon monoxide radiolysis: relevance to comets, icy satellites, and interstellar ices. *Icarus, 140*, 451- 461.

Johnson, R.E., Carlson, R.W., Cooper, J.F., Paranicas, C., Moore, M.H., & Wong, M.C., (2004), Radiation effects on the surfaces of the Galilean satellites, in F. Bagenal, T. Dowling, W. McKinnon (Eds.), *Jupiter. The planet, satellites and magnetosphere*, Cambridge, UK: Cambridge University Press.

Joy, D.C., & Luo, S., (1989). An empirical stopping power relationship for low-energy electrons. *Scanning*, 11, 176-180.

Knoll, G.F., (2010), *Radiation detection and measurements*, 4th ed., NJ: John Wiley & Sons.

Kolawa, E., Balint, T., Birur, G., Bolotin, G., Brandon, E., Del Castillo, L., et al., (2007), *Extreme environment technologies for future space science missions* (Tech. Rep. JPL D-32832), Pasadena, CA: Jet Propulsion Laboratory.

Kriss, A.A., & Hamby, D.M., (2004). Beta spectroscopy with a large-area avalanche photodiode module and a plastic scintillator. *Nuclear Instruments and Methods in Physics Research A, 525*, 553-559.

Ladzianský, M., Šagátová, A., Nečas, V., Dubecký, F., & Linhart, V., (2009). Deep traps study of radiation-damaged semi-insulating GaAs detectors introduced by neutrons. *Nuclear Instruments and Methods in Physics Research A, 607*, 135-137.

Lane, A.L., Nelson, R.M., & Matson, D.L., (1981). Evidence for sulphur implantation in Europa's UV absorption band. *Nature*, *292*, 38.

Linder, D.R., Coates, A.J., Woodliffe, R.D., Alsop, C., Johnstone, A.D., Grande, M., et al., (1998), *The Cassini CAPS electron epectrometer*, in R.F. Pfaff, J.E. Borovsky, D.T. Young (Eds.), *Measurement techniques in space plasmas: particles* (p. 257), Washington, DC: American Geophysical Union.

Lioliou, G., & Barnett, A.M, (2015). Electronic noise in charge sensitive preamplifiers for X-ray spectroscopy and the benefits of a SiC input JFET. *Nuclear Instruments and Methods in Physics Research A*, *801*, 63-72.

Lioliou, G., & Barnett, A.M., (2016). Gallium arsenide detectors for X-ray and electron (beta particle) spectroscopy. *Nuclear Instruments and Methods in Physics Research A*, *836*, 37-45

Lioliou, G., Meng, X., Ng, J.S., & Barnett, A.M., (2016). Temperature dependent characterization of gallium arsenide X-ray mesa p-i-n photodiodes. *Journal of Applied Physics*, *119*, 124507.

Lioliou, G., Whitaker, M.D.C., & Barnett, A.M., (2017). High temperature GaAs X-ray detectors. *Journal of Applied Physics*, *122*, 244506.

Liu, Y.-p., Tang, X.-b., Xu, Z.-h., Hong, L., Wang, H., Liu, M., & Chen, D., (2015). Influences of planar source thickness on betavoltaics with different semiconductors. *Journal of Radioanalytical and Nuclear Chemistry*, *304*, 517-525.

Livi, S.A., McNutt, R., Andrews, G.B., Keath, E., Mitchell, D., & Ho, G., (2003). The Energetic Particles Spectrometers (EPS) on MESSENGER and New Horizons. *American Institute of Physics Conference Proceedings*, *679*, 838-841.

Ly Anh, T., Perd'ochová, A., Nečas, V., & Pavlicová, V., (2006), Radiation resistance study of semi-insulating GaAs-based radiation detectors to extremely high gamma doses, *Nuclear Physics B - Proceedings Supplements*, *150*, 402-406.

Mauk, B.H., Haggerty, D.K., Jaskulek, S.E., Schlemm, C.E., Brown, L.E., Cooper, S.A., et al., (2013). The Jupiter Energetic Particle Detector Instrument (JEDI) investigation for the Juno mission. *Space Science Reviews*, *213*, pp. 1-58.

Mazzillo, M., Sciuto, A., Catania, G., Roccaforte, F., & Raineri, V., (2012). Temperature and light induced effects on the capacitance of 4H-SiC Schottky photodiodes. *IEEE Sensors Journal*, *12*, 1127-1130.

McCord, T.B., Hansen, G.B., Matson, D.L., Johnson, T.V., Crowley, J.K., Fanale, F.P., et al., (1999). Hydrated salt minerals on Europa's surface from the Galileo Near-Infrared Mapping Spectrometer (NIMS) investigation. *Journal of Geophysical Research: Planets*, *104*, 11827-11851.

McNutt, R.L., Livi, S.A., Gurnee, R.S., Hill, M.E., Cooper, K.A., Andrews, G.B., et al., (2008). The Pluto Energetic Particle Spectrometer Science Investigation (PEPSSI) on the New Horizons mission. *Space Science Reviews*, *140*, 315-385.

Neudeck, P.G., Okojie, R.S., & Chen, L.-Y., (2002). High-temperature electronics - a role for wide bandgap semiconductors?. *Proceedings of the IEEE*, 90, 1065-1076.

Novara, M., (2001). The BepiColombo Mercury Surface Element. *Planetary and Space Science*, 49, 1421-1435.

Owens, A., (2012), *Compound semiconductor radiation detectors*, Boca Raton, FL: CRC Press.

Paranicas, C., Carlson, R.W., & Johnson, R.E., (2001). Electron bombardment of Europa. *Geophysical Research Letters, 28*, 673-676.

Paranicas, C., Cooper, J.F., Garrett, H.B., Johnson, R.E., & Sturner, S.J., (2009), *Europa's radiation environment and its effects on the surface*, in R.T. Pappalardo, W.B. McKinnon, K.K. Khurana (Eds.), *Europa* (pp. 529-545), Tuscon, AZ: University of Arizona Press.

Press, W.H., Teukolsky, S.A., Vetterling, W.T., & Flannery, B.P., (1986), *Numerical Recipes*, Cambridge, UK: Cambridge University Press.

Paskowitz, M.E., & Scheeres, D.J., (2006). Design of science orbits about planetary satellites: application of Europa. *Journal of Guidance, Control, and Dynamics, 29*, 1147-1158.

Phillips, C.B., & Chyba, C.F., (2001). *Impact gardening rates on Europa: comparison with sputtering*. Paper presented at 32nd Annual Lunar and Planetary Science Conference, Houston, TX.

Powell, J., Powell, J., Maise, G., & Paniagua, J., (2005). NEMO: A Mission to search for and return to Earth possible life forms on Europa. *Acta Astronautica, 57*, 579-593.

Rossi, L., Fischer, P., Rohe, T., & Wermes, N., (2006), *Pixel detectors: from fundamentals to applications* (p. 123), Berlin, Germany: Springer-Verlag.

Roth, L., Saur, J., Retherford, K.D., Strobel, D.F., Feldman, P.D., McGrath, M.A., & Nimmo, F., (2014). Transient water vapor at Europa's south pole. *Science, 343*, 171-174.

Šagátová, A., Zat'ko, B., Pavlovič, M., Sedlačková, K., Hybler, P., Dubecký, F., & Nečas, V., (2014). GaAs detectors irradiated by low doses of electrons. *Journal of Instrumentation, 9*, C04036.

Schötzig, U., (2000). Half-life and X-ray emission probabilities of ^{55}Fe. *Applied Radiation and Isotopes, 53*, 469-472.

Sparks, W.B., Hand, K.P., McGrath, M.A., Bergeron, E., Cracraft, M., & Deustua, S.E., (2016). Probing for evidence of plumes on Europa with HST/STIS. *The Astrophysical Journal, 829*, 121.

Swinyard, B.M., Joy, K.H., Kellett, B.J., Crawford, I.A., Grande, M., Howe, C.J., et al., (2009). X-ray fluorescence observations of the Moon by SMART-1/D-CIXS and the first detection of Ti Kα from the lunar surface. *Planetary and Space Science*, 57, 744-750.

Sze, S.M., & Ng, K.K., (2007), *Physics of semiconductor devices*, 3rd ed, Hoboken, NJ: John Wiley & Sons.

Tatsuhiko, U., Takao, K., Masahiro, T., Satoshi, T., Takeshi, I., & Katsuyoshi, T., (2010). Detection efficiency of plastic scintillator for Gaseous Tritium sampling and measurement system. *Fusion Engineering and Design, 85*, 1474-1478.

Ulrici, J., Fischer, P., Klein, P., Lutz, G., Neeser, W., Richter, R., et al., (2005). Imaging performance of a DEPFET pixel bioscope system in Tritium autoradiography. *Nuclear Instruments and Methods in Physics Research A, 547*, 424-436.

Vampola, A.L., (1998), *Measuring energetic electrons-what works and what doesn't,* in R.F. Pfaff, J.E. Borovsky, D.T. Young (Eds.), *Measurement techniques in space plasmas: particles* (p. 339), Washington, DC: American Geophysical Union.

Vapirev, E.I., Sueva, D., Spassov, V., Chikov, N., & Ivanov, I., (1994). Detection of β-particles, conversion electrons and γ-rays with silicon planar detectors. *Applied Radiation and Isotopes*, *45*, 453-459.